Characterization of necking phenomena in high speed experiments by using a single camera

Gilles Besnard, Jean-Michel Lagrange, François Hild, Stéphane Roux, Christophe Voltz

Characterization of necking phenomena in high speed experiments by using a single camera

Gilles Besnard,[1,2] Jean-Michel Lagrange,[1] François Hild,[2,*] Stéphane Roux,[2] Christophe Voltz[3]

[1]CEA, DAM, DIF, F-91297 Arpajon, France

[2]LMT-Cachan, ENS Cachan / CNRS / UPMC / UniverSud Paris 61 avenue du Président Wilson, F-94235 Cachan Cedex, France

[3]CEA, DAM, Is-sur-Tille, France

[*]Corresponding author: hild@lmt.ens-cachan.fr

Abstract

The purpose of the experiment described herein is the study of material deformation (here a cylinder) induced by explosives. During its expansion, the cylinder (initially 3 mm thick) is thinning until fracture appears. Some tens of microseconds before destruction, strain localizations occur and induce mechanical necking. To characterize the time of first localizations, 25 stereoscopic acquisitions at about 500,000 frames per second are used by resorting to a single ultra-high speed camera. The 3D reconstruction from stereoscopic movies is described. A special calibration procedure is followed, namely, the calibration target

is imaged during the experiment itself. To characterize the performance of the present procedure, resolution and optical distortions are estimated. The principle of stereoscopic reconstruction of an object subjected to a high speed experiment is then developed. This reconstruction is achieved by using a global image correlation code that exploits random markings on the object outer surface. The spatial resolution of the estimated surface is evaluated thanks to a realistic image pair synthesis. Last, the time evolution of surface roughness is estimated. It gives access to the onset of necking.

Keywords: detonics, necking, stereovision, ultra high speed camera.

1 Introduction

For detonics applications, objects subjected to very high deformations (about 50 to 100 % strains) are to be observed in very short times (i.e., less than 100 μs). To characterize the phenomenon of necking and to compare experimental results with hydrodynamic computations, ultra-fast cinematography is very useful. This diagnostic, which is resolved in space and time, is used to monitor external surfaces of expanding objects. For the present applications, dedicated cameras are used [1]. Thanks to a stereoscopic setup, 3D reconstructions are possible.

The stereovision technique is used for mechanical observations. Numerous applications exist for quasi static experiments [2, 3, 4, 5] where stereovision is coupled with digital image correlation [6]. The latter is a non-intrusive measurement technique that provides a large density of measurement points.

Thanks to the generalization of digital cameras (with CCD or CMOS sensors), the use of stereo-correlation tends to develop in the field of fast dynamics such as, for example, torsion and tensile tests on Hopkinson bars [7, 8]. However, the use of stereovision for quantitative purposes for high-speed experiments is marginal. Recently it was shown that the use of stereovision to monitor detonics tests [9, 10] is possible with CCD cameras. However, the lack of resolution of these sensors (typically, 312×260 pixels at 10^6 fps) is a strong limitation. In the present study, film cameras with a revolving mirror are used. They have a very high resolution (e.g., 2000×1500 pixels at 10^6 fps). However, additional treatments are necessary because of the digitization of the developed film and the specific technology of these cameras.

The objective of the present paper is to provide a characterization of the surface quality of the object, and the time of inception of localized phenomena. First, the experimental setup is presented. Because of the use of a specific optical chain, the implemented techniques are introduced and characterized (resolution and distortions). Then, the stereovision coupled with digital image correlation is presented. A synthetic case is analyzed to determine the detection resolution (i.e., the minimum defect size). Last, in order to improve the quality of the 3D reconstruction, a correction method which allows for large displacements is presented. The whole procedure is finally illustrated to analyze a true experiment.

2 Stereovision principle

This first part deals with the reconstruction of an object based upon stereoscopic observations. The principle of formation of images via mirrors and a rotating mirror framing camera and its calibration are introduced. The specific global digital image correlation algorithm used to perform stereo-matching is finally presented.

2.1 Formation of images via mirrors

Mirrors are very useful tools in the field of vision and their shape can be designed to meet various specifications [11, 12, 13]. Several angles of view with the *same* camera are possible. In this part, theoretical expressions of the transformation matrix, i.e., relating the 3D coordinates of a point of the scene and its projection in the image plane are recalled. This is performed within the framework of an orthographical model with mirror, which is an appropriate model for the measurements performed herein since the object size is very small (height: 100 mm, diameter: 100 mm, see Figure 1(a)) in comparison with the distance between the camera and the object (ca. 16 m).

Because of the large optical path between the camera and the object (about 16 m), image formation is split into two stages, illustrated in two dimensions in Figure 1(a). This process is identical for the two mirrors and only the generic case is considered in the sequel. Let Q be a point in the image scene. It is imaged at point Q'' by mirror (P). The orthogonal projection of Q'' onto the image plane is denoted by $\tilde{q}''$.

To establish the relationship in a 3D setting, the various transformations depicted in Figure 2 are considered. The reference frame of the scene is related to that of the image. Let Ω be the origin in the image plane. For any point M, $\boldsymbol{x}_M$ denotes the vector position in the image frame. The mirror is defined by its normal $\boldsymbol{n}$ and its center O. The mirror plane (P) is defined by the following equation for any point M belonging to the mirror

$$\boldsymbol{n} \cdot (\boldsymbol{x}_M - \boldsymbol{x}_O) = \boldsymbol{n}\boldsymbol{x}_M + d = 0 \tag{1}$$

with $d = -\boldsymbol{n} \cdot \boldsymbol{x}_O$.

Point Q' is the orthogonal projection of Q on (P), so that

$$\boldsymbol{x}_{Q'} - \boldsymbol{x}_Q = k\boldsymbol{n} \tag{2}$$

where k is the distance QQ'

$$k = -(\boldsymbol{n} \cdot \boldsymbol{x}_Q + d) \tag{3}$$

Point Q'' is the symmetric of Q with respect to plane (P) and its position is given by

$$\boldsymbol{x}_{Q''} = \boldsymbol{x}_Q - 2(\boldsymbol{n} \cdot \boldsymbol{x}_Q + d)\boldsymbol{n} \tag{4}$$

Using homogeneous coordinates, the above relationship can be written in a matrix form

$$\begin{pmatrix} x_{Q''} \\ y_{Q''} \\ 1 \end{pmatrix} = \begin{bmatrix} -2n_x^2 & -2n_x n_y & -2n_x n_z & -2n_x d \\ -2n_x n_y & -2n_y^2 & -2n_x n_z & -2n_y d \\ 0 & 0 & 0 & 1 \end{bmatrix} \begin{pmatrix} x_Q \\ y_Q \\ z_Q \\ 1 \end{pmatrix} \equiv \mathbf{P} \begin{pmatrix} x \\ y \\ z \\ 1 \end{pmatrix} \tag{5}$$

The transformation from the mirror image to the camera is a classical problem [11]. Usually, it is decomposed into three elementary operations [14],

namely, a projection matrix $\mathbf{P}$ associated with the orthographic projection model

$$\mathbf{P} = \begin{bmatrix} \pi & 0 & 0 & 0 \\ 0 & \pi & 0 & 0 \\ 0 & 0 & 0 & 1 \end{bmatrix} \tag{6}$$

where π is the magnification coefficient, matrix $\mathbf{K}$ expressing the transformation between the retinal coordinates in the retinal plane of the camera (in metric units) and the pixel coordinates in the image, and a matrix $\mathbf{A}$ associated with the transformation between the camera coordinate system and the reference coordinate system, attached to the object in the present case

$$\mathbf{A} = \begin{bmatrix} r_{11} & r_{12} & r_{13} & t_x \\ r_{21} & r_{22} & r_{23} & t_y \\ r_{31} & r_{32} & r_{33} & t_z \\ 0 & 0 & 0 & 1 \end{bmatrix} \quad , \quad \mathbf{K} = \begin{bmatrix} k_u & 0 & u_0 \\ 0 & k_v & v_0 \\ 0 & 0 & 1 \end{bmatrix} \tag{7}$$

where k_u and k_v are scale factors (horizontally and vertically and r_{ij} and t_k are rotation and translation parameters). The combination of these matrices yields

$$\begin{pmatrix} u \\ v \\ 1 \end{pmatrix} = \mathbf{KPA} \begin{pmatrix} X \\ Y \\ Z \\ 1 \end{pmatrix} \tag{8}$$

with $(X, Y, Z, 1)$ the homogeneous coordinates of Q in the reference frame. Last, the sought relationship reads

$$\begin{pmatrix} u \\ v \\ 1 \end{pmatrix} = \begin{bmatrix} m_{11} & m_{12} & m_{13} & m_{14} \\ m_{21} & m_{22} & m_{23} & m_{24} \\ 0 & 0 & 0 & 1 \end{bmatrix} \begin{pmatrix} X \\ Y \\ Z \\ 1 \end{pmatrix} \equiv \mathbf{M} \begin{pmatrix} X \\ Y \\ Z \\ 1 \end{pmatrix} \tag{9}$$

where the parameters m_{ij} denote the coefficients of the transformation matrix $\mathbf{M}$, whose expression is simplified compared with those obtained in the case of pinhole model [6]. In the present case, $m_{3i} = 0$ for $i = 1, 2, 3$ and $m_{34} = 1$ [14].

2.2 Calibration and stereoscopic reconstruction

In the following, the calibration technique that provides the coefficients of matrix $\mathbf{M}$ is introduced. A calibration target is designed with a collection of known reference points $\boldsymbol{x}^\alpha$ where $\alpha = 1, ..., N$ whose position is determined by using a co-ordinate measuring machine and an optical microscope leading to a 10 μm uncertainty. Their image coordinates $\boldsymbol{u}^\alpha$ are identified. The relationship $\boldsymbol{u}^\alpha = \mathbf{M}\boldsymbol{x}^\alpha$ is exploited to determine $\mathbf{M}$ using a least squares optimization strategy. The objective function to minimize is defined as

$$\mathcal{O}(\mathbf{M}) = \sum_\alpha \|\mathbf{M}\boldsymbol{x}^\alpha - \boldsymbol{u}^\alpha\|^2 \tag{10}$$

enforcing the condition $m_{34} = 1$ [14].

Introducing matrix $\boldsymbol{\Xi}_{ij} = x_i^\alpha x_j^\alpha$, the elements of matrix $\mathbf{M}$ read

$$m_{ij} = (\boldsymbol{\Xi})_{ik}^{-1} . \left(x_k^\alpha u_j^\alpha\right) \tag{11}$$

The expected conditions $m_{3i} = 0$ for $i = 1 - 3$ can be checked as a self-consistent validation of the calibration. It is worth noting that with the model used herein, the coefficients $m_{31},\ m_{32},\ m_{33}$ are vanishingly small.

In practice, the calibration is carried out by putting a 3D target near the observed object (Figure 3). The calibration using a planar object successively positioned at various positions [15] is not possible in the present experiment. Only one image is necessary to calibrate the system. This approach (i.e., *in situ* calibration target) is implemented since lighting is obtained by pyrotechnic flashes that are only used during the experiment itself. The latter further requires that the explosive be introduced only at the very end of the experiment preparation, for safety reasons. Prior to that, the position of various objects (the mirrors in particular) may change slightly because of operator manipulations. Therefore, the calibration target has to remain in the field of view (and hence will be destroyed during the explosion). Therefore, the proposed camera calibration procedure is not "optimal" in the sense that all the field of view is not calibrated. However, it will shown in Section 4.2 that the distortions remain small, thereby only having a small impact on the quality of the reconstruction.

Once the calibration has been carried out, the coordinates of the considered point in the 3D object frame $\boldsymbol{X}^t = (X, Y, Z)$ are over-determined by the corresponding left and right image coordinates $\boldsymbol{U}^t = (u_l, v_l, u_r, v_r)$. A least squares minimization is used to relate $\boldsymbol{X}$ to $\boldsymbol{U}$, which is written as

$$\boldsymbol{X} = (\mathbf{C}^t\mathbf{C})^{-1}\mathbf{C}^t(\boldsymbol{U} - \boldsymbol{D}) \tag{12}$$

with

$$\mathbf{C} = \begin{pmatrix} m_{11}^l & m_{12}^l & m_{13}^l \\ m_{21}^l & m_{22}^l & m_{23}^l \\ m_{11}^r & m_{12}^r & m_{13}^r \\ m_{21}^r & m_{22}^r & m_{23}^r \end{pmatrix} \quad , \quad \boldsymbol{D} = \begin{pmatrix} m_{14}^l \\ m_{24}^l \\ m_{14}^r \\ m_{24}^r \end{pmatrix} \tag{13}$$

where m_{ij}^l (resp. m_{ij}^r) are the coefficients of the left (resp. right) transformation matrix.

2.3 Registration by digital image correlation

The reconstruction is possible only if the points of the right image correspond to those of the left image. It becomes necessary to register spatially and temporally all the points. This is carried out by resorting to Digital Image Correlation (DIC), which consists in following the position of a random pattern in a sequence of images. This technique has the advantage of offering a much denser field of reconstruction than that provided by point tracking. Position uncertainty of the image-points is less than 0.1 pixel for the present applications. An example of speckle and grid in the case of cylinder expansion is shown in Figure 4. DIC principle is to register the gray levels of two images, one being the reference $f(\boldsymbol{x})$ and the other the deformed one, $g(\boldsymbol{x})$ with $\boldsymbol{x} = (x, y)$. The brightness conservation is given by

$$g(\boldsymbol{x}) = f(\boldsymbol{x} + \boldsymbol{u}(\boldsymbol{x})) \tag{14}$$

The technique used herein is global and consists in expanding the displacement $\boldsymbol{u}(\boldsymbol{x})$ onto a basis of (known) functions $\Psi_n(\boldsymbol{x})$

$$\boldsymbol{u}(\boldsymbol{x}) = \sum_n a_{\alpha n} \Psi_n(\boldsymbol{x}) \boldsymbol{e}_\alpha \tag{15}$$

where $a_{\alpha n}$ are the sought parameters associated with basis vectors $\boldsymbol{e}_\alpha$. The displacement field is then found by carrying out the global minimization of the following functional

$$\|f(\boldsymbol{x}+\boldsymbol{u}(\boldsymbol{x}))-g(\boldsymbol{x})\|_\Omega^2 \tag{16}$$

by resorting to multi-scale linearizations / corrections [16] using the following Taylor expansion up to the first order of $f(\boldsymbol{x}+\boldsymbol{u}(\boldsymbol{x}))$

$$f(\boldsymbol{x}+\boldsymbol{u}(\boldsymbol{x}))=f(\boldsymbol{x})+\boldsymbol{u}(\boldsymbol{x}).\boldsymbol{\nabla} f(\boldsymbol{x}) \tag{17}$$

so that linear systems have to be solved

$$\begin{aligned}\left[\iint_\Omega \partial_\alpha f(\boldsymbol{x})\Psi_m(\boldsymbol{x})\partial_\beta f(\boldsymbol{x})\Psi_n(\boldsymbol{x})\mathrm{d}\boldsymbol{x}\right] a_{\beta n} = \\ \iint_\Omega \{g(\boldsymbol{x})-f(\boldsymbol{x})\}\partial_\alpha f(\boldsymbol{x})\Psi_m(\boldsymbol{x})\mathrm{d}\boldsymbol{x}\end{aligned} \tag{18}$$

where ∂_α and ∂_β are the partial derivatives with respect to α and β. System (18) is written in a more compact way as

$$\mathbf{S}\boldsymbol{a}=\boldsymbol{b} \tag{19}$$

where $\boldsymbol{a}$ is the vector containing the coefficients to be determined. In the following, so called Q4-DIC [16] is used in which a mesh made of 4-noded quadrilateral (Q4) elements are used for which a bilinear interpolation is used to describe the displacement field in each element. The main interest is that continuity of the displacement field is introduced, which offers larger robustness and a greater number of measurement points for the same uncertainty level [16].

3 Experimental setup

The experiment reported herein aims at studying the mechanical behavior of copper under high speed loading conditions. The material is a high purity copper (UNS C10100 - ISO Cu-OFE grade). The studied object is a cylinder (length: 100 mm, internal diameter: 100 mm, wall thickness: 3 mm). Different forming steps are needed to obtain the final sample. First, a thick blank is deep drawn to a cup form. Second, the cylinder is turned by flospinning. Last, the hemispherical top of the piece is cut out and the cylindrical part is kept. The final microstructure is obtained by a heat-treatment to trigger recrystallization and stress relaxation. The average grain size is 25 μm (this value is constant in both directions). The external surface is polished to ensure good reflectivity for laser velocimetry measurements.

Two high-speed rotating-mirror framing LCA cameras are used to record optical images of the dynamically expanding cylinder (Figure 5). The first one (70 mm film, and 25 images) is utilized for the observation of the whole experiment (mainly to analyze plastic instabilities and to measure the external shape). The second one (35 mm film, and 25 images) is dedicated to stereovision. For both cameras the frame rate is 500,000 fps (or 2 μs interframe, time of exposure: 700 ns) so that the sequence is approximately 60 μs long. Since it is impossible to synchronize precisely two cameras of that type for stereovision, observation recordings are performed by utilizing two mirrors (Figure 1). Consequently, two views of the expanding object are exposed on the same film. The mirrors make an angle of 12°. This value is chosen for practical reasons to allow the two views to be recorded in the same picture. The firing sequence is started when the rotating mirrors of the

two cameras coincide. Three argon lights ($150 \times 150 \times 900$ mm^3) illuminate the scene, the illumination duration is about 100 μs. They are initiated at a reference time t_0 set at detonator ignition. In the present paper, all times are counted with the time origin set to t_0.

4 Characterization of the optical chain

Rotating mirror framing film cameras are used for quantifications of local (necking) phenomena. The latters are observed via a random pattern that must be characterized. If the random pattern is too fine, there is not enough contrast (i.e., small gradients) and the resolution of the correlation procedure is not sufficient. Conversely, if the speckle is too coarse, large element sizes are needed so that the number of measurement points decreases. The optimal size of the pattern is used in the synthetic case described in Section 5.1. Moreover, the cameras used herein are complex since they are made of a principal lens, 25 secondary lenses and many mirrors are used to form an image. These optical devices may generate distortions that are to be characterized.

4.1 Resolution

A resolution calibration target, similar to a Foucault pattern, is put in place of the object. The former consists of 6 small plates joined together to form a 300×450 mm^2 plate. The pattern consists of a succession of horizontal and vertical lines with varying thicknesses ranging from 0.6 mm to 1.4 mm with a 0.1 mm step. The center of the plate is then put in place of the observed

object (located at a distance of 16 m from the camera) and at an angle of 40° with respect to the optical axis to estimate the depth of field.

The 25 images acquired by the camera have been compared visually. In view of the absence of any variation, only one image of the sequence was analyzed. The step of digitization is 10 μm in the film plane so that the physical size of one pixel is equal to 220 μm in the object plane. The image is then filtered out to remove luminous heterogeneities caused by an imperfect lighting. The result is shown in Figure 6.

The resolution of the optical chain is sought to assess the minimum size that can be observed, and the size of the random pattern to be deposited for an optimal observation. To quantify this size, contrast of each line is analyzed to deduce the cut-off frequency corresponding to 50 % of the dynamic range. The latter is obtained by analyzing a zone close to the edges of the plate and by rescaling the amplitudes between 0 and 1. Local contrast is obtained in an identical way for horizontal and vertical lines.

To increase the signal to noise ratio, the local contrast of each set of lines of the resolution target is obtained by averaging the realigned pattern (after corrections of residual rotations ensuring perfect horizontality or verticality of the transitions). This average is performed over 50 pixels for the vertical direction and 1,000 pixels for the horizontal one. In Figure 7(a), the change of the gray level is shown for two sizes, namely, 1.4 mm and 1 mm, with a loss of contrast appearing for the smallest marking size.

In Figure 7(b), variations of contrast that would be obtained if the calibration target were seen through a linear optical system of Gaussian transfer function of Full Width at Middle Height (FWMH) ranging from 0.5 to

3.9 mm, are plotted in solid lines. These values are given for magnifications of about 20. The experimental curve lies between the lines corresponding to an FWMH of 1.1 and 1.3 mm, meaning that it will be difficult to distinguish correctly elements smaller than these two sizes. Thus, the speckle deposited onto the cylinder must have at least a diameter of 1.2 mm. This characterization is useful for the realistic synthesis of images discussed in Section 5.1.

4.2 Lens distortions

Because of the use of a rotating mirror framing camera and many mirrors between the object and the camera, the estimation of optical distortions is an important step in the experiments. Techniques utilized to determine the distortions of the *whole* optical system require the acquisition of one image per secondary lens. It is different from procedures followed to analyze quasi static experiments [17] or even for the case of a dynamic test [18]. Moreover, because of the complexity of the optical chain, it is not possible to project the distortions found onto a polynomial basis as generally performed [17, 6]. In the present case, the frame-to-frame distortions were found negligible with respect to that of the whole optical chain.

The proposed approach to correct for optical distortions consists in resorting to a random numerical texture that is printed onto a plate by laser engraving. The plate and its support are put on a stool. Then, pictures of the plate are shot by the camera. A correlation computation is run between the digital reference and the first image acquired by the camera. This computation, carried out by the technique presented in Section 2.3, provides a

displacement field (u_{tot}, v_{tot}) containing all the information concerning magnification, in- and out-of-plane rotation (a first order approximation can be used in the present case since the distance of the object to the camera is very large), and distortions. To account for these different components, the displacement field is projected onto the following basis

$$\begin{aligned} U_{aff} &= ax + by + c \\ V_{aff} &= dx + ey + f \end{aligned} \tag{20}$$

The distortion field corresponds to the displacement residuals. The type of image obtained in the present case is shown in Figure 8(a) for a theoretical image shown in Figure 8(b). The junction between the two mirrors gives rise to spurious results. Consequently, the distortions are evaluated independently for the left and right mirrors (Figure 9(a) and 9(b)). The amplitudes of the distortions remain small, namely, mean value in the centipixel range, standard deviation in the pixel range, and no particular pattern is caused by the piece of adhesive tape seen in Figure 8(a). Consequently, the influence of optical distortions on the stereoscopic reconstruction of the object are neglected. The fields of distortions are similar for the 25 images of the sequence [19], thereby proving that the frame-to-frame distortions are of secondary influence. Last, no artifacts related to digitization (e.g., discontinuities between successive lines perpendicular to the scan direction) were observed in the analyses performed in the present section. If any, they remain very small in comparison with those induced by the optical chain.

5 Application

In this part, the stereovision technique is applied to analyze a cylinder expansion caused by blast loading. It is worth noting that other types of loading configurations have been used in the literature [20, 13]. First, a synthetic case representative of the experiment is studied to estimate the performances of the technique and in particular the resolution of the reconstruction. This enables for the evaluation of the minimum size of observable and quantifiable defects. In the present experiments, the observed surface undergoes important deformations (beyond 100 % strain). This is the reason why the computation is not carried out with the initial reference but rather with an updated reference that causes a cumulation of measurement errors. A reduction in the size of the reconstructed surface is observed since the points that leave the initial region of interest are not taken into account. To improve the performances of the approach, a pre-correction for large displacements is performed. It consists in seeking a uniform translation to apply to the images so that, on average, the region of interest is motionless. Then the DIC algorithm is run using the prior translation as an initialization of the displacement field. This procedure makes the computation faster, more stable and more accurate. Finally, the stereovision technique is applied to the experiment itself [21, 22, 23, 24].

5.1 Detection level

Before applying the stereo-correlation procedure to an experimental case, it is important to evaluate the size and amplitude of defects that can be detected.

The hydrodynamic code HESIONE [25] predicts the shape of the specimen at different stages of evolution. For any instant of time, t, the predicted surface is projected onto the actual surface by least squares minimization.

Figure 10(a) shows one picture of the specimen in its reference state. The surface texture is artificially created by mimicking laser marking (i.e., with parallel rays) based on a computerized pattern. The picture of the surface deformed by the computed displacement field, and onto which the original surface marking has been projected is shown in Figure 10(b). In addition to the smooth displacement field, some additional perturbations are superimposed to check the resolution of the analysis. They would correspond to localized "bumps" of various diameters (0.5, 1, 5, 10 and 30 mm), and amplitudes (0.125, 0.25, 0.5, 1, 2.5 and 5 mm) as illustrated in Figure 10(c). A total of 15 different perturbations are introduced.

Based on the knowledge of the transformation matrix, each point of the 3D surface is projected onto the two image planes to create synthetic left and right stereoscopic image pairs as close as possible to experimental images. When compared with the experimental geometry, the mean distance between the projection into the image of a known 3D point and the corresponding image-point extracted in the image is equal to ± 5 pixels. The blurring effect of the entire optical chain is taken into account through convolution with a Gaussian filter. 16 image pairs are generated, one of them (witness) containing no perturbation. Two examples of left-right pairs are shown in Figure 11(a-d) and (b-e). To appreciate the effect of the bumps on the images, the same figure shows the difference between two similar images with and without the perturbations. Figure 11(c) and (f) correspond respec-

tively to the left and right views. It is to be emphasized that no noise has been added to the images in order to focus on detection issues.

A DIC analysis was performed on those artificial images, based on the same choice of parameters as the one used in the experiment, namely, 16×16 pixel elements are selected based on the signal to noise ratio. A comparison between the measured and prescribed displacements for each bump allows for the evaluation of the resolution. To carry out this analysis, the measured and imposed shapes are unfolded onto a plane as suggested by Luo and Riou [26].

Figure 12(a) shows the prescribed perturbation for the easiest cases (amplitudes of 2.5 mm and 5 mm, left and right respectively, for a 30 mm diameter bump), while Figure 12(b) is the measured shape. In spite of a large noise affecting the shape of the bump, this perturbation is rather well captured by DIC computations. Figures 12(c) and 12(d) correspond to smaller perturbations (amplitudes of 125 μm and 250 μm, left and right respectively, for a 5 mm diameter). Although the perturbations are detected, their sizes and amplitudes cannot be estimated reliably. The reason for this lies in the intrinsic resolution of the DIC analysis performed here with elements of size 16 pixels, or 2.9 mm. Thus the entire bump can fit in a two element wide square. A summary of the results is presented in Figures 13(a) and 13(b) where measured amplitudes and diameters respectively, normalized by the prescribed counterpart, are shown for all tested cases.

It is concluded that for very severe experimental conditions (rotating mirror high speed camera at 16 m optical distance from the specimen, magnification of 22, small radius of curvature, and poorly contrasted surface texture) the limit of detection of such bumps is of the order of 5 mm, and a

minimum size of about 10 mm is needed to allow for a reliable quantification of the perturbation. Moreover, 250 μm amplitudes are resolved reliably for those conditions. These conclusions hold for a fixed element size of 16 pixels. Smaller elements lead to too noisy measurements to secure the determination, whereas larger elements are too coarse. This level is to be compared with the 3D reconstruction uncertainty achieved herein. A level of 90 μm is estimated by randomly perturbing the position of the calibration points, and reconstructed points with realistic values [19].

Possible improvements involve drastic changes in the experimental set-up. CCD camera could offer images in digital format directly, thus limiting the digitation step in the analysis. However access to similar pixel sizes still represents a technical challenge. A better resolution could also be obtained through a higher magnification, at the expense of a smaller frame.

5.2 Large displacement handling

In the context of detonics, very high strain levels between consecutive images have to be captured. This fact is a major difficulty for DIC. A specific procedure has been designed to allow for a much more robust analysis in this context. As a side benefit, displacement fields appear to be less subjected to noise.

The principle of the method is simply to initialize the DIC analysis, which is in the present case an iterative procedure, by a prior determination of the displacement field obtained via a simulation of the experiment. This allows for a convergence of the displacement determination into the deepest minimum, and avoid trappings into secondary minima. Let us note that a

multi-scale strategy is adopted in the DIC analysis for the same purpose of limiting secondary minima trappings [16]. However, at the largest scales the contrast of the images is significantly reduced and hence some nodes or zones may be polluted by such artifacts. In contrast, a fair prior estimate of the displacement field, which may still be inaccurate, requires DIC to address only the remaining corrections displacements, and hence can be tackled with less coarsened images. As this procedure only affects the initial displacement field, it does not affect the final one at convergence as can be checked by perturbing this prior determination, and checking that the final determination is unaffected. This robustness allows for some tolerance on the quality of this first displacement field, and hence, small effects such as the motion of the cylinder axis are neglected.

In the DIC procedure, the deformed image is corrected at each iteration by the current determination of the displacement field. Hence, any displacement field can be used at initialization, and no subsequent modification of the DIC algorithm is needed. When the initial field is close to the final solution, convergence is fast and accurate. The only operation needed is to transform the 3D displacement field from HESIONE code [25] into both the right and left 2D displacement fields used for the time registration of the DIC procedure. This projection is performed as in the previous subsections using the transformation matrices introduced in Section 2 once the 3D frames used in the code and in the stereo-correlation procedure coincide. This is achieved by a least squares minimization between the initial experimental and numerical shapes. A mispositioning error of the order of 1 mm is achieved. Figure 14 illustrates the effect of the prior correction of a late image onto

the reference one. It can be seen that most of the displacement has been accounted for, and only small differences remain to be determined (by DIC). When this prior determination is not taken into account, a larger element size (24 pixels) has to be chosen to limit the uncertainty level. With the present initialization, a 16 pixel element can be dealt with.

5.3 Experimental reconstruction

After the experiment, the film composed of 25 acquisitions is developed and the 25 images are digitized independently from each other. From the fixed elements of the scene (yellow paper in Figure 1(a) or the calibration target shown in Figure 14) repositioning of images is performed by adjusting a translation correction so that the elements remain motionless [19].

Reconstruction of the surface is given in Figure 15 for three different times. In these figures, the result of the stereo-correlation is shown in blue, while the computed one (given by HESIONE) is in red. Apart from some slight positioning differences between experimental and computed geometries, the two surfaces superimpose quite well for the entire duration of the experiment. Displacement corrections of at most ± 20 pixels need to be measured. With the multi-scale algorithm used herein this level is easily measured. Moreover, in the last picture, a clear defect can be identified, which is interpreted as a local thinning of the specimen, i.e., an example of necking. The image pair shown in Figure 16 supports that statement.

In order to investigate on a quantitative basis the onset of necking, it is proposed to base the analysis on the standard deviation of the normal surface displacements. This standard deviation can be seen as a measure of

the roughness of the expanding surface, which is expected to remain small for a uniform strain of the surface, and to display a sudden increase when necking (at least necking that can be captured by the DIC analysis, i.e., at a large enough scale). The standard deviation is expected to be sensitive to the sampled surface as the lower part of the specimen is subjected to a larger strain. Thus the standard deviation is estimated over three regions, namely, first globally over the entire field of analysis, second over a central zone (where edge effects are avoided), and third on a zone located at the bottom of the specimen where necking is seen to occur first.

The first two standard deviations are shown as functions of time (through the image number) in Figure 17(a). A steady increase is observed with an acceleration taking place for the two last stages, although the level of fluctuation of this curve makes this last observation questionable. The central zone shows a smaller roughening, which is consistent with the lower strain level reached in this zone. Let us emphasize the fact that the displacement field is computed from the reference image to the current one, and hence the steady increase cannot be attributed to a cumulation of measurement errors. Note also that the initial image has already a significant roughness because it has suffered a significant expansion prior to be captured in the first image. The third standard deviation computed over the bottom part of the specimen is shown in Figure 17(b). The sudden acceleration of the standard deviation for the last images seems to depart clearly from the previous steady evolution and supports the previous discussion on a detectable necking occurring in this zone. This also supports the idea that the global standard deviation is affected by the necking of the lower part, and that the sudden rise is actually

meaningful. Moreover, the a priori uncertainty is estimated to amount to 0.5 pixel, or 90 μm. The impact of image noise has been estimated to amount to an additional 100 μm [19]. The sum of these uncertainties is well below the fluctuation level reported in those graphs.

6 Conclusion

A successful attempt is reported to reconstruct complex 3D displacement fields for high-speed blast experiments under very severe experimental conditions using a rotating mirror high speed camera. Both large scale shape changes as well as local features associated with necking can be captured. The techniques were also set up to estimate the resolution and distortions of the optical chain allowing for the analysis of a synthetic case representative of the experimental test.

Specific procedures useful to enhance the performance of such stereo-correlation analyses have been developed. In particular, the combination of pre-corrections and global digital image correlation algorithm provides both robust and accurate 2D displacement fields that are suitable to stereo-correlation to get three dimensional displacement fields. Other directions for improving the experiment itself are currently being investigated, namely, surface marking, which can sustain the very strain rates of the specimen, sub-microsecond lighting and digital cameras [27, 28] that will in a near future replace the film camera used in the present study. In the same spirit, combining more than two views of the same scene is a stimulating direction for increasing the accuracy of the reconstruction even with images having a low contrast

or specular reflections that may always occur unexpectedly [29, 14, 30]. Stereovision is thus a very powerful tool to analyze high-speed experiments.

Last, let us note that the fact that the observed object is initially cylindrical makes the DIC procedures difficult due to the perspective issues. An a priori knowledge on the initial shape of the object would make the reconstruction step easier and faster. It would also allow to further increase the reconstructed surface area.

References

[1] S.F. RAY. High speed photography and photonics. *SPIE*, 1997.

[2] P.F. LUO, Y.J. CHAO, and M.A. SUTTON. Application of stereo vision to three-dimensional deformation analyses in fracture experiments. *Optical Engineering*, 33 no. 3: 981–990, 1994.

[3] P.F. LUO and F.C. HUANG. Application of stereo vision to the study of mixed-mode crack-tip deformations. *Optics and Lasers in Engineering*, 33: 349–368, 2000.

[4] Z. LEI, H.T. KANG, and G. REYES. Full field strain measurement of resistant spot welds using 3D image correlation. *Experimental Mechanics*, 50 no. 1: 111–116, 2010.

[5] J.-J. ORTEU. 3-D Computer Vision in Experimental Mechanics. *Optics and Lasers in Engineering*, 47 no. 3-4: 282–291, 2009.

[6] M.A. SUTTON, J.J. ORTEU, and H.W. SCHREIER. Image correlation for shape, motion and deformation measurements: Basic Concepts, Theory and Applications. *Springer*, 2009.

[7] F. BARTHELAT, Z. WU, B.C. PROROK, and H.D. ESPINOSA. Dynamic torsion testing of nanocrystalline coatings using high-speed photography and digital image correlation. *Experimental Mechanics*, 43 no 3: 331–340, 2003.

[8] A. GILAT, T. SCHMIDT, and J. TYSON. Full field measurement during a tensile split Hopkinson bar experiment. *Journal de Physique 4*, 134: 687–692, 2006.

[9] V. TIWARI, M.A. SUTTON, S.R. McNEILL, S. XU, X. DENG, W.L. FOURNEY, and D. BRETALL. Application of 3D image correlation for full-field transient plate deformation measurements during blast loading. *International Journal of Impact Engineering*, 36: 862–874, 2009.

[10] P.J. REU and T.J. MILLER. The application of high-speed digital image correlation. *Journal of Strain Analysis*, 43: 673–688, 2008.

[11] F. DEVERNAY. Vision stéréoscopique et propriétés différentielles des surfaces. PhD dissertation, École Polytechnique, 1997.

[12] L. DUVIEUBOURG, S. AMBELLOUIS and F. CASTESTAING. Single-camera stereovision setup with orientable optical axes. *Computational Imaging and Vision*, 32: 173-178, 2005.

[13] H. ZHANG and K. RAVI-CHANDAR. Nucleation of cracks under dynamic loading. *12 International Conference on Fracture*, 2009.

[14] O. FAUGERAS. Three-dimensional computer vision, a geometric viewpoint. *MIT Press*, 1993.

[15] M. DEVY, V. GARRIC, J.-J. ORTEU. Camera calibration from multiple views of a 2D object, using a global non linear minimization method. IEEE/RSJ International Conference on Intelligent Robots and Systems (IROS'97), Grenoble (France), 7-11 September 1997.

[16] G. BESNARD, F. HILD, and S. ROUX. Finite-element displacement fields analysis from digital images: application to Portevin-Le Chatelier bands. *Experimental Mechanics*, 46: 789–803, 2006.

[17] D. GARCIA. Mesure de formes et de champs de déplacements tridimensionnels par stéréo-corrélation d'images. PhD dissertation, École des Mines d'Albi, 2001.

[18] V. TIWARI, S.R. McNEILL, and M.A. SUTTON. Assessement of high speed imaging systems for 2D and 3D deformation measurements: methodology development and validation. *Experimental Mechanics*, 47: 561–579, 2007.

[19] G. BESNARD. Caractérisation et quantification de surfaces par stéréocorrélation pour des essais mécaniques du quasi statique à la dynamique ultra-rapide. PhD dissertation, École Normale Supérieure de Cachan, 2010.

[20] K. RAVI-CHANDAR, A.B. ALBRECHT, H. ZHANG, and K. M. LIECHTI. High strain rate adhesive behavior of polyurea coatings on aluminum. *12th International Conference on Fracture*, 2009.

[21] G. BESNARD, S. ROUX, F. HILD, and J.M. LAGRANGE. Contact-free characterization of materials used in detonic experiments. *34th International Pyrotechnics Seminar Europyro*, 2: 815–824, 2007.

[22] G. BESNARD, J.M. LAGRANGE, F. HILD, S. ROUX, and C. VOLTZ. Métrologie pour l'expérimentation en détonique, accès au phénomène de striction. *Neuvième colloque international francophone du club SFO/CMOI, Nantes*, 2008.

[23] G. BESNARD, B. ETCHESSAHAR, J.M. LAGRANGE, C. VOLTZ, F. HILD, and S. ROUX. Metrology and detonics: analysis of necking. *28th International Congress on High-Speed Imaging and Photonics*, 7126: 71261N–1–71261N–12, 2008.

[24] C. VOLTZ, J.M. LAGRANGE, G.BESNARD, and B. ETCHESSAHAR. Application of ultra-high-speed optical observations and high-speed X-ray radiography measurements to the study of explosively driven copper tube expansion. *28th International Congress on High-Speed Imaging and Photonics*, 7126: 71261M–71261M10, 2008.

[25] HESIONE: CEA-DAM 3D Hydrodynamic code.

[26] P.F. LUO and S.S. LIOU. Measurement of curved surface by stereo vision and error analysis. *Optics and Lasers in Engineering*, 30: 471–486, 1998.

[27] *http://www.cordin.com/products.html.*

[28] *http://www.shimadzu.com/products/test/hsvc/index.html.*

[29] N. AYACHE and F. LUSTMAN. Trinocular sterovision for robotics. *INRIA report*, 1086, 1989.

[30] R. HARTLEY and A. ZISSERMAN. Multiple View Geometry in Computer Vision. Cambridge University Press, 2004.

List of Figures

(a) (b)

Figure 1: Visualization of the stereoscopic system (a). Reference mirrors in which the cylinder and the calibration target can be seen. Above the mirrors, the pyrotechnic flashes are located in wood cases. Model of image formation in the case of two mirrors of reference and with an orthographic model (b).

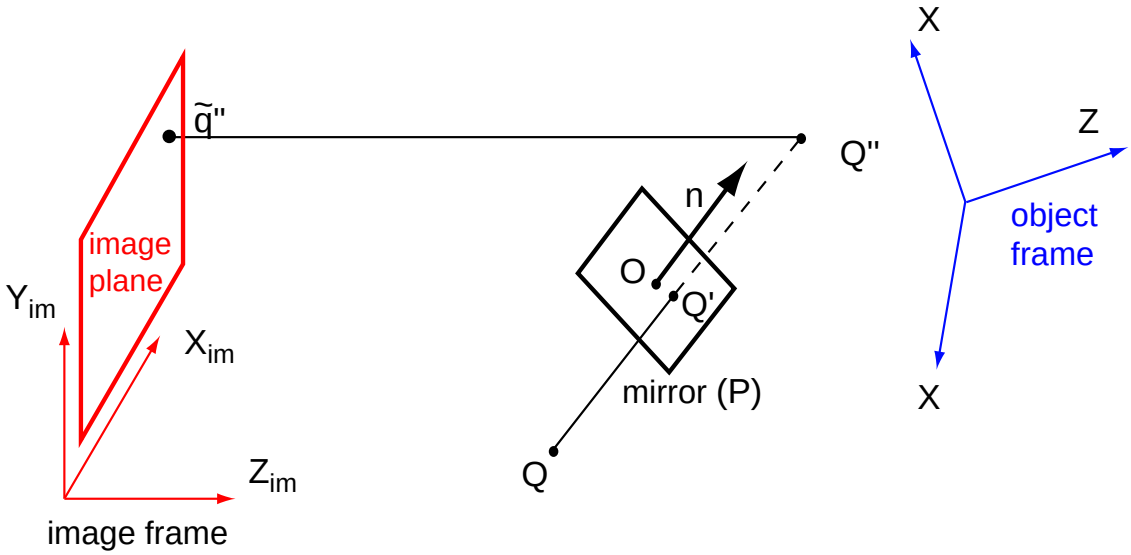

Figure 2: Model of image formation via a mirror P of normal $\boldsymbol{n}$.

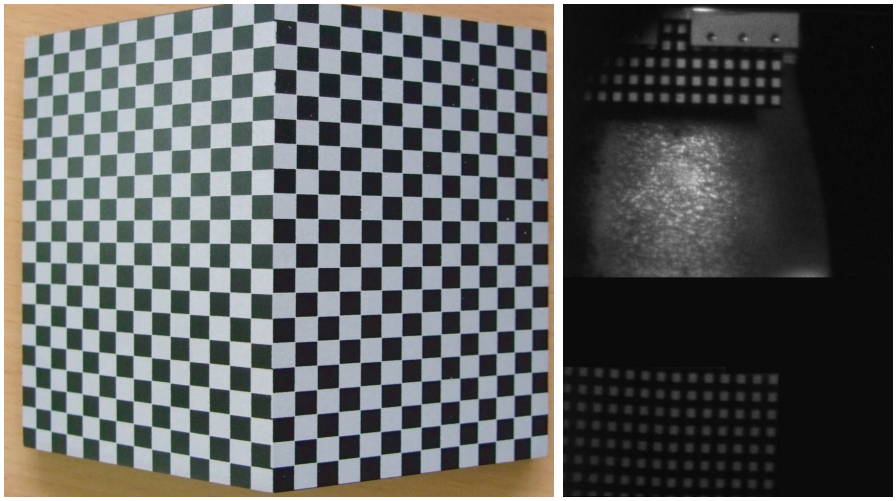

(a) (b)

Figure 3: Calibration target (a) and its positioning on the experimental stage (b). The centers of the white squares are automatically detected after a local thresholding and a calculation of the barycenters of the detected related components. The calibration is performed by matching the image coordinate of those centers and their 3D counterparts.

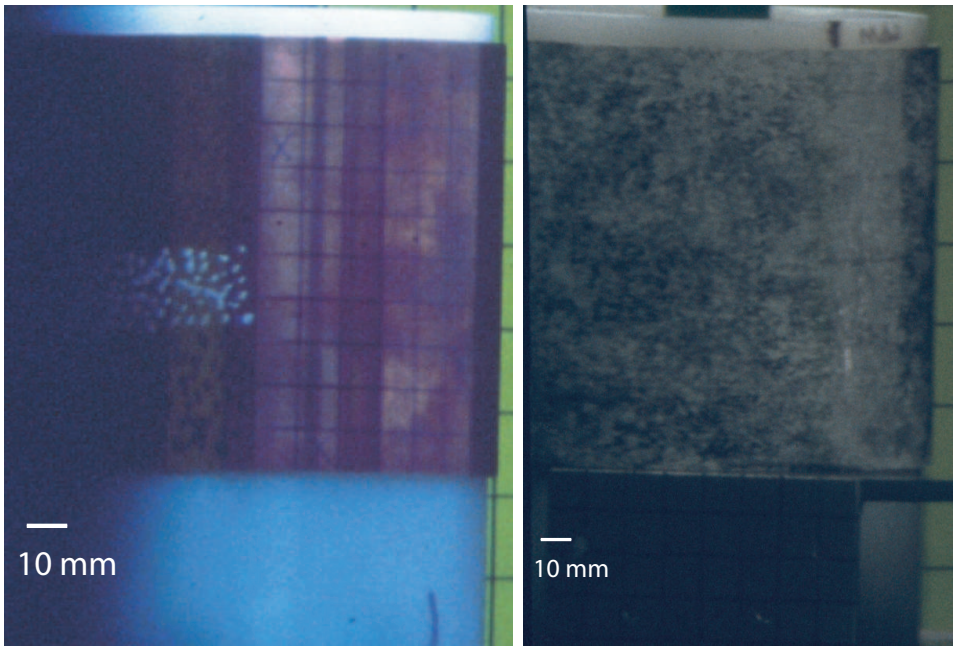

(a) (b)

Figure 4: Visualization of different markings: with grid (a) or speckle (b).

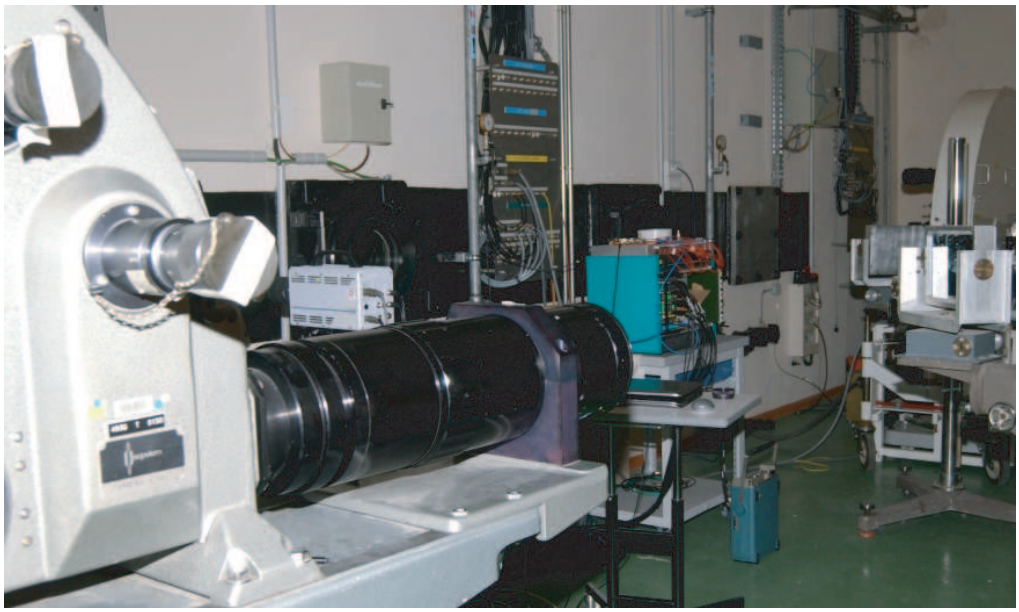

Figure 5: High-speed cameras in the room dedicated to detonics experiment instrumentation.

Figure 6: Image of the resolution calibration target filtered by a low frequency Gaussian filter to remove the heterogenous illumination.

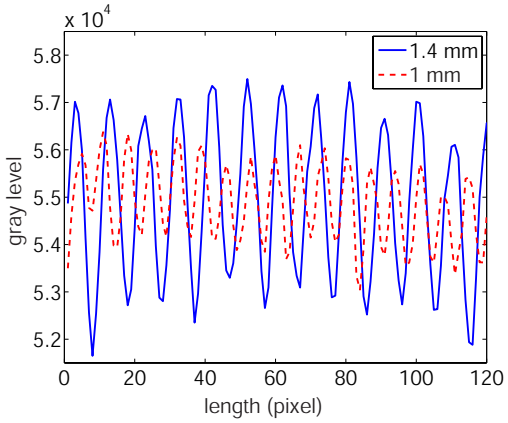

(a)

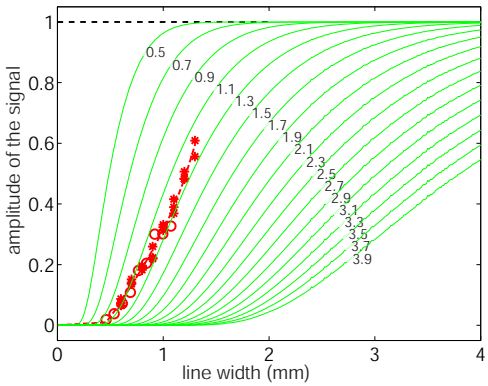

(b)

Figure 7: (a) Evolution of gray level contrast with the spatial period of the crenels . (b) Normalized contrast versus line width : experimental points (red symbols) and curves (green) obtained for a linear system with a Gaussian transfer function of varying FWMH from 0.5 to 3.9 mm.

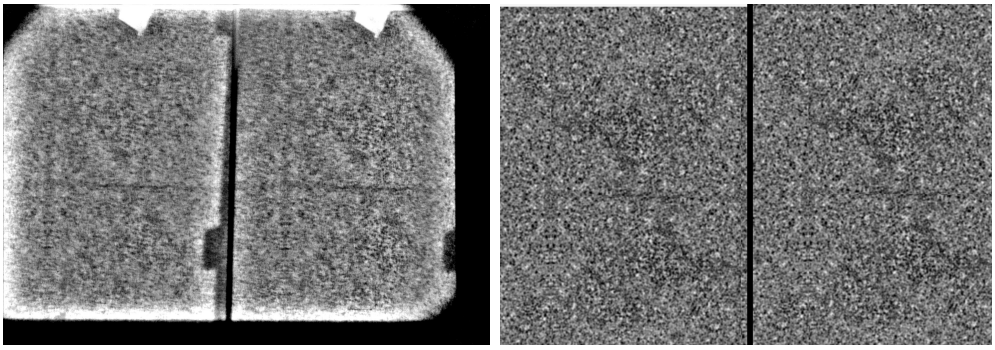

(a) (b)

Figure 8: Image obtained with stereoscopic mirrors and used for estimating of distortions (a). The white rectangle located on the upper edge of the field corresponds to a piece of adhesive tape used to fix the calibration pattern onto the machine support. Digital images printed on the calibration plate (b). The distorsions of the whole optical chain is assessed by registering the left and right parts of both pictures.

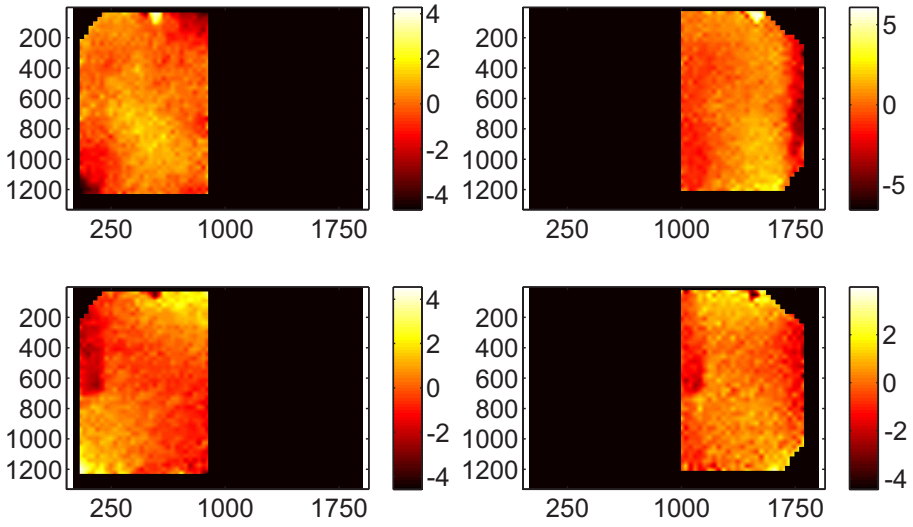

(a) (b)

Figure 9: Measured distortion taking into account the stereoscopic mirrors, left (a) and right (b) mirrors. The color scale encodes the magnitude of the displacement expressed in pixel (1 pixel = 180μm). The top (resp. bottom) figures show the displacement component along the longitudinal (resp. transverse) axis.

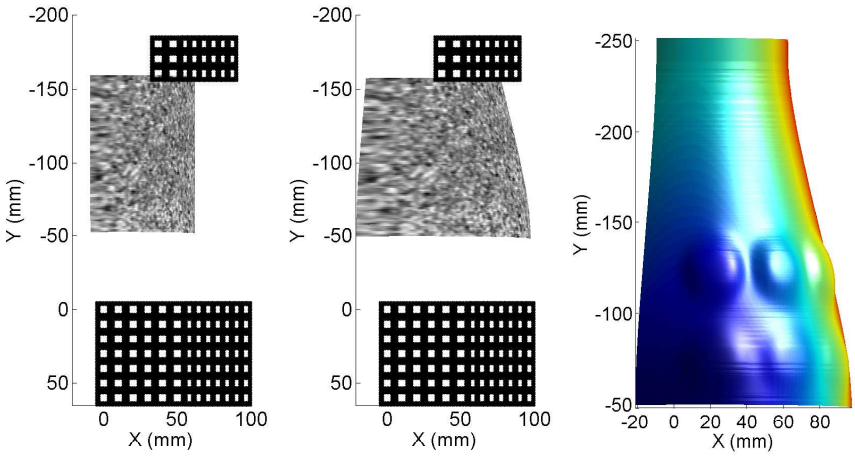

(a) (b) (c)

Figure 10: Reference configuration created by mimicking laser marking (a), deformed surface with a known displacement field (b). Addition of local bump defects on the deformed surface (c).

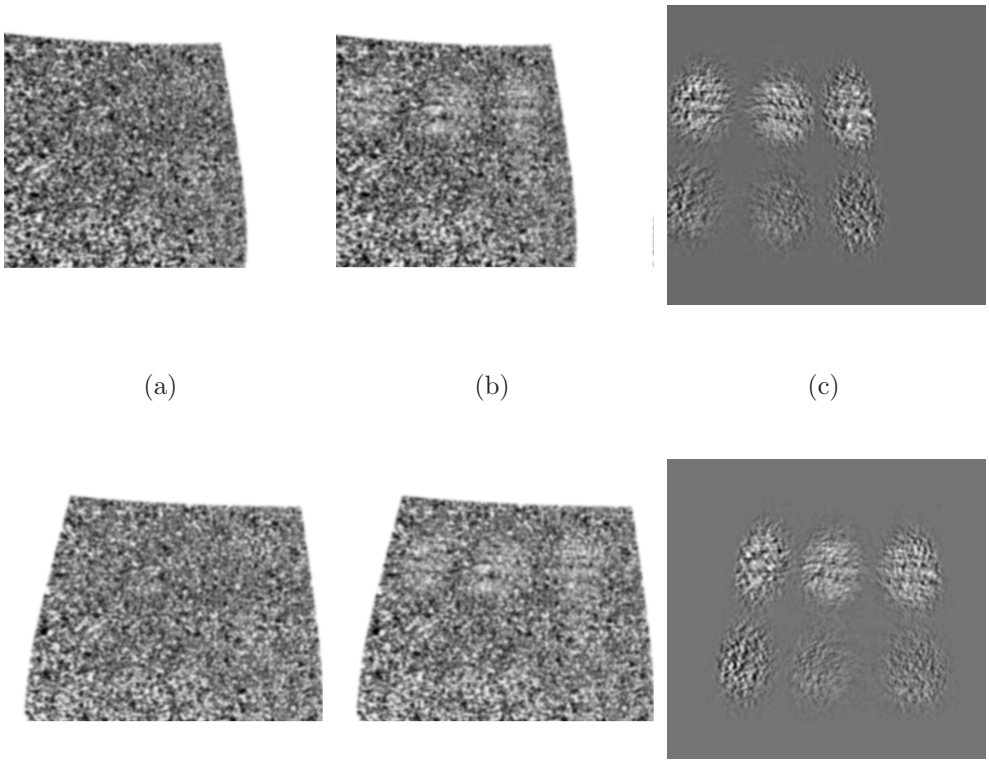

(a) (b) (c)

(d) (e) (f)

Figure 11: 3D surface rendering when unfolded onto a plane. Reference (a) and deformed (b) left images, and their difference (c). Reference (d) and deformed (e) right images, and their difference (f).

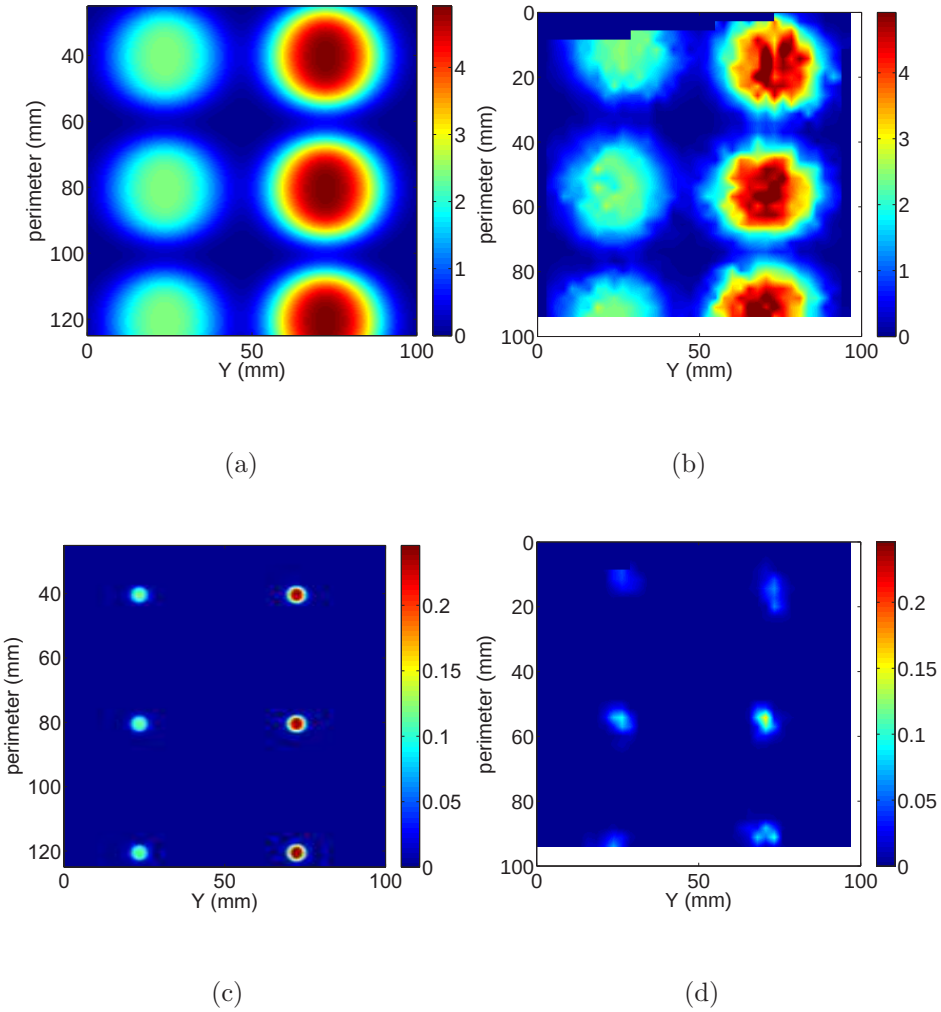

Figure 12: Comparison between the imposed (unfolded) surface displacement (left) and as determined from stereo-reconstruction from synthetic images (right). The top figures show bumps of 30 mm diameter, and 2.5 mm or 5 mm amplitudes. The bottom figures show bumps of 5 mm diameter, and 125 μm or 250 μm amplitudes.

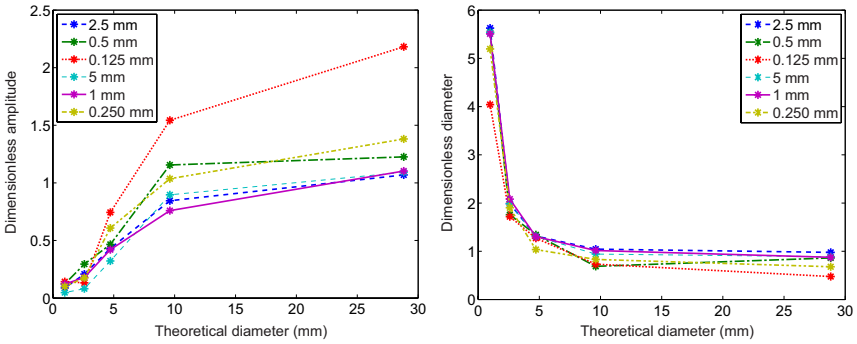

(a) (b)

Figure 13: Estimated amplitude (normalized by the imposed one) vs. diameter for different amplitudes (a). Estimated diameter (normalized by the imposed one) vs. diameter for different amplitudes (b).

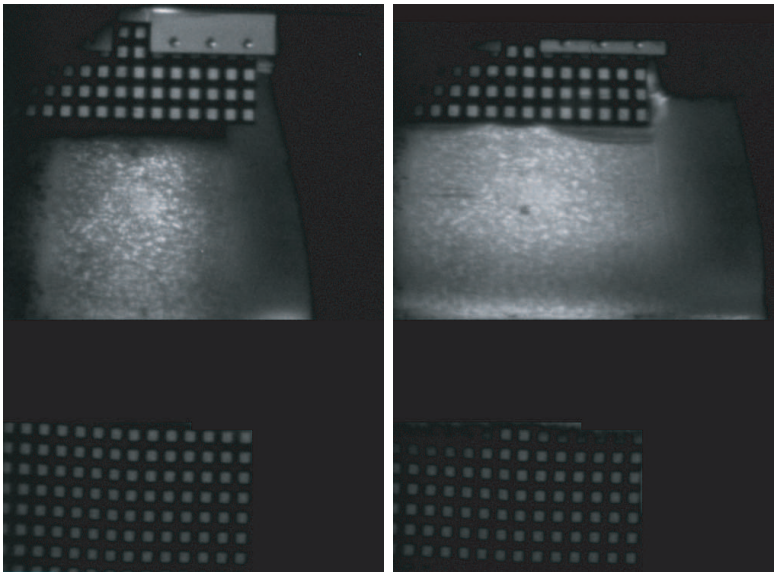

(a) (b)

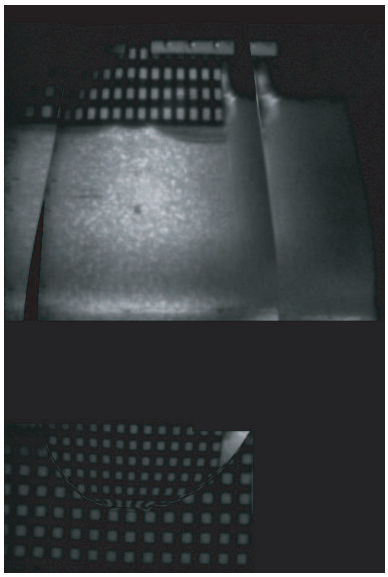

(c)

Figure 14: Illustration of the pre-correction: (a) reference image number 13 (b) raw image number 24, (c) corrected image number 24.

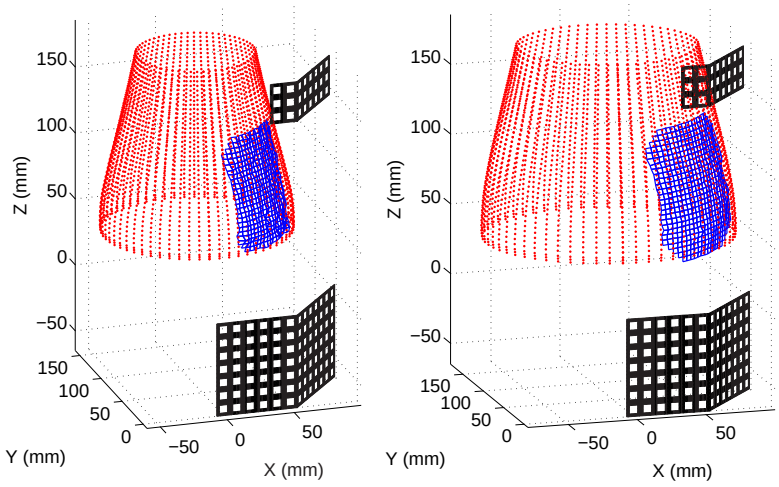

(a)

(b)

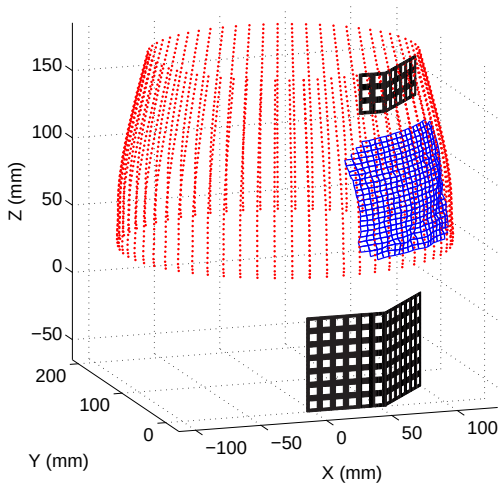

(c)

Figure 15: Reconstruction of the specimen surface at three stages of expansion, image no. 6 (a), image no. 13 (b) and image no. 25 (final one)(c). The deformed mesh represents the reconstruction data while the points represent the interpolated surface.

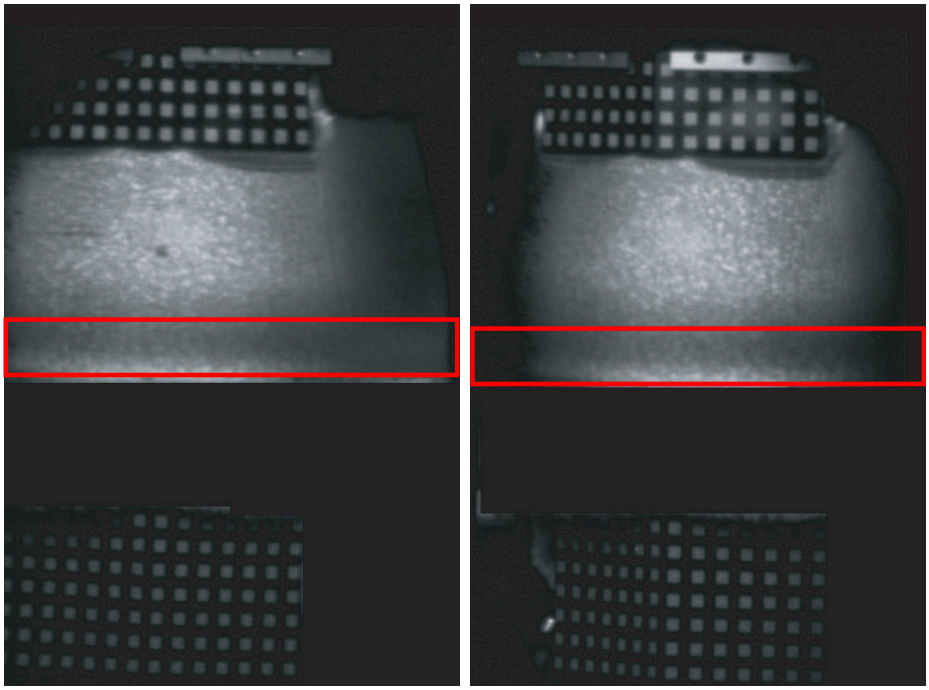

(a) (b)

Figure 16: Last image pair (left and right views). On the lower part (inside the red rectangle), a necking appears.

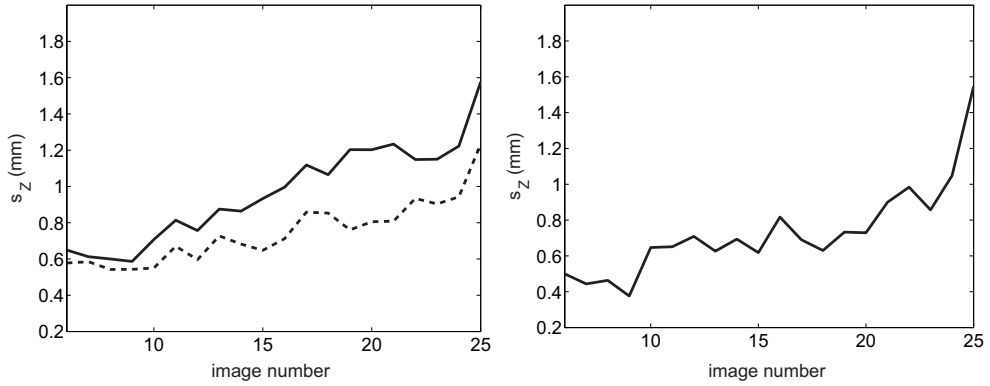

(a) (b)

Figure 17: Evolution of surface roughness, evaluated over the entire surface or a central zone total zone (plain curve), on a central zone (dotted curve) (a) and locally (b)